

Article

Experimental Comparison of Methods to Evaluate Heat Generated by Magnetic Nanofluids Exposed to Alternating Magnetic Fields

Elisabetta Sieni ^{1,*}, Simonetta Geninatti Crich ², Maria Rosaria Ruggiero ², Lucia Del Bianco ³, Federico Spizzo ³, Roberta Bertani ⁴, Mirto Mozzon ⁴, Marco Barozzi ⁵, Michele Forzan ⁴ and Paolo Sgarbossa ⁴

¹ Department of Theoretical and Applied Sciences, University of Insubria, 21100 Varese, Italy

² Department of Molecular Biotechnologies and Health Sciences, University of Turin, 10126 Torino, Italy

³ Department of Physics and Earth Science, University of Ferrara, 44122 Ferrara, Italy

⁴ Department of Industrial Engineering, University of Padova, 35131 Padova, Italy

⁵ Department of Science and High Technology, University of Insubria, 22100 Como, Italy

* Correspondence: elisabetta.sieni@uninsubria.it

Abstract: The paper aims to compare different methods able to estimate the specific loss power (SLP) generated by three different types of magnetic nanoparticles, MNPs, dispersed in a suspension fluid, e.g., octane or water. The nanoparticles were characterized morphologically in terms of shape and size, chemically for composition and their physical properties like magnetization and SLP were studied. We evidenced the differences in SLP evaluation due to the applied method, particularly in the presence of thermally induced phenomena such as aggregation or precipitation of MNPs that can affect the heating curve of the samples. Then, the SLP determination methods less sensible to this phenomenon appear to be the ones that use the initial slope when the sample is in quasi-adiabatic condition. Finally, we propose a comparison of those methods based on the pros and cons of their use for the SLP determination of magnetic nanofluids. In particular, the analysis of the behavior of the heating curve is useful to evaluate the useful amplitude of the interval analysis for the initial slope methods.

Keywords: magnetic nanoparticles; SLP; hyperthermia; thermal characterization



Citation: Sieni, E.; Geninatti Crich, S.; Ruggiero, M.R.; Del Bianco, L.; Spizzo, F.; Bertani, R.; Mozzon, M.; Barozzi, M.; Forzan, M.; Sgarbossa, P. Experimental Comparison of Methods to Evaluate Heat Generated by Magnetic Nanofluids Exposed to Alternating Magnetic Fields. *Fluids* **2023**, *8*, 83. <https://doi.org/10.3390/fluids8030083>

Academic Editor: Mehrdad Massoudi

Received: 23 December 2022

Revised: 15 February 2023

Accepted: 23 February 2023

Published: 27 February 2023



Copyright: © 2023 by the authors. Licensee MDPI, Basel, Switzerland. This article is an open access article distributed under the terms and conditions of the Creative Commons Attribution (CC BY) license (<https://creativecommons.org/licenses/by/4.0/>).

1. Introduction

Magnetic fluid hyperthermia (MFH) uses magnetic nanofluids, i.e., magnetic nanoparticles suspended in a liquid medium, to increase the local temperature in a target area. The magnetic nanoparticles can generate heat when they are exposed to a time-varying magnetic field [1–7]. Hyperthermia can be an effective anticancer agent, particularly when combined with ionizing radiation or chemotherapy [8]. Thermal stress, depending upon the time of exposure and temperature, can directly initiate cell death or cause intracellular protein damage, denaturation, or degradation. If the affected proteins are enzymes involved in DNA damage repair, hyperthermia can effectively inhibit or abrogate cancer cell recovery from DNA-damaging agents. Further, physiological factors enhance the susceptibility of tumors to combined heat and radiation because mild tissue heating promotes vasodilation which increases blood flow to raise pO₂ which increases the biological effectiveness of the (low linear energy transfer) radiation. In general, an increment of a few degrees with respect to the physiological temperature of 37 °C, i.e., a final temperature between 41 and 43 °C, is able to induce cell death by apoptosis [4,5,9–15]. A higher temperature can induce necrosis and this effect is used, for instance, in ablation therapy [3,16,17], as it is well known the magnetic field used in the MFH is in the order of 10^2 kA/m (in a range that corresponds to 50–200 Oe) at 100–400 kHz [1–3,18–22]. In general, the maximum frequency

and field amplitude are limited by considerations of patient safety due to off-target Joule heating caused by induced eddy currents [23]. In fact, importantly for human exposure, it is pivotal to maintain the product of the magnetic field strength (H) and its frequency (f) below a threshold safety value. This is known as the Brezovich criterion, for which the product $C = H \times f$ should remain below 5×10^8 A/(ms) to minimize any collateral effects of alternating magnetic fields on the human body. In recent years this limit was updated and now the safety limit commonly prescribed is set at 5×10^9 A/(ms) [24], even though some authors suggest that it could be raised close to 10^{10} A/(ms) [25,26].

The specific loss power, SLP, is used as a parameter to investigate how much energy is absorbed per magnetic nanoparticles mass (NPs) under AMF. Hence, extensive efforts have been made to produce magnetic nanomaterials possessing high SLP values. In fact, different types of magnetic nanoparticles (MNPs) could be synthesized using iron oxide, Mn-Fe oxide, or CoFe compounds [18,27–31]. These types of MNPs could be produced by physical or chemical processes. The most common chemical methods for MNP production include co-precipitation and thermal decomposition [32–37]. These different materials show different magnetic characteristics and consequently generate a different power density expressed in terms of SLP. The variation in SLP values can be attributed to several factors including sample size, concentrations, and magnitude and frequency of the applied field [7,38–41].

The SLP generated by an MNP fluid could be estimated from calorimetric data using different methods as largely discussed in the literature [7,40,42–47]. The simplest method includes the evaluation of the fit of a long acquisition of the temperature vs time curve using an exponential model (named in some literature reference as the Box-Lucas model [46–48]), typical of heating phenomena for which the initial part of the curve has a quasi-adiabatic behavior. This method requires time for each acquisition and a stable environmental temperature [45,48]. The other two methods involve the computation of the slope of the temperature curve considering the interval in which temperature rises linearly and in which the quasi-adiabatic condition is valid [9,43–45,48–54]. These methods require less time for data acquisition since the quasi-adiabatic interval is within the first few minutes of the fluid heating curve. In this paper, we compare the SLP values obtained using these three different computation methods to a variety of MNP samples. The SLP evaluation using the fit of the exponential model was performed at a single frequency and a single magnetic field intensity (e.g., see [48]); whereas the two methods that involve the slope of the temperature curve were used to characterize the different MNPs in terms of SLP at three different frequencies and different magnetic field intensities [44,45,48,55]. We also provide the data obtained from the physical characterizations of the MNPs to highlight the similarities and differences arising from the synthesis methods. In particular, the samples are different in terms of size, magnetic properties, metal ions content, and generated power density. In our study, we considered three MNPs based either on iron-oxide prepared by co-precipitation, C5 sample, or by thermal decomposition, sample C12, and a sample based on Mn-Fe oxide, labeled C26. All the NPs powders were suspended in water while one, C5, was also suspended in octane.

2. Materials and Methods

Iron(III) acetylacetonate (99.9%), manganese(II) acetylacetonate (99.9%), oleylamine ($\geq 98\%$), oleic acid ($\geq 99\%$), 1,2-tetradecanediol (90%), benzyl ether (98%), cetyltrimethylammonium bromide ($\geq 98\%$), iron(II) chloride tetrahydrate ($\geq 99\%$), iron(III) chloride hexahydrate ($\geq 99\%$), ammonium hydroxide solution (28.0–30.0% NH_3 basis), n-octane (98%), and solvents were purchased from Sigma-Aldrich and used without further purification.

2.1. Synthesis of the Nanoparticles

The magnetic nanoparticles used in this study have been prepared by common thermal decomposition of organometallic precursors or coprecipitation by slight modification of reported methods [34,56].

2.1.1. Synthesis of C26

In a typical preparation, 2.80 g (7.90 mmol) of iron(III) acetylacetonate, $[\text{Fe}(\text{acac})_3]$, and 1.00 g (3.95 mmol) of manganese(II) acetylacetonate, $[\text{Mn}(\text{acac})_2]$, were mixed in an inert atmosphere (N_2) with oleylamine (6.40 g, 24.0 mmol), oleic acid (6.80 g, 24.0 mmol), and 1,2-tetradecanediol (9.20 g, 36.0 mmol) in 100 mL of benzyl ether as solvent. The dark red homogeneous mixture was magnetically stirred and heated at 200 °C for 120 min and then at 300 °C for 60 min. After cooling the system to room temperature, the black suspension was poured into a 3-fold volume of ethanol and mechanically stirred. The NPs were magnetically separated, washed three times with ethanol (50 mL), and dried under vacuum. For dispersion in water, an equal mass of cetyltrimethylammonium bromide (CTAB) was ground with the NPs until a homogeneous mixture was obtained and dispersed in deionized water.

2.1.2. Synthesis of C12

In a similar procedure as for C26, 2.80 g (7.90 mmol) of iron(III) acetylacetonate, $[\text{Fe}(\text{acac})_3]$, were mixed in an inert atmosphere (N_2) with oleylamine (6.40 g, 24.0 mmol), oleic acid (6.80 g, 24.0 mmol), and 1,2-tetradecanediol (9.20 g, 36.0 mmol) in 100 mL of benzyl ether as solvent. Reaction time, temperature, purification procedure, and dispersion in water were performed as in the synthesis of C26.

2.1.3. Synthesis of C5

This sample was prepared by a coprecipitation method starting from inorganic salts in basic solution. Typically, iron(II) chloride tetrahydrate (4.97 g, 25.0 mmol) and iron(III) chloride hexahydrate (13.52 g, 50.0 mmol) are dissolved in deionized water (150 mL) and treated with a solution of ammonium hydroxide (24% in water). The base is added under vigorous mechanical stirring until pH 11 (controlled with litmus paper) and subsequently, 7.5 mL of oleic acid (6.70 g, 23.7 mmol) is added to the black suspension and the temperature is increased to 60 °C and maintained for 30 min. The black solid is separated magnetically, washed with water several times and then three times with ethanol (50 mL), and dried under vacuum.

2.2. Nanofluid

The nanofluids were obtained by suspending the NPs powder in either an apolar solvent (n-octane) or deionized water. Due to the use of lipophilic surface functionalization of the NPs, they are easily dispersible in apolar solvents such as hydrocarbons, while the use of a surfactant is necessary for their dispersion in polar solvents and water. For this reason, the dispersion in n-octane (chosen for its relatively low volatility, to reduce the effect of vaporization on its temperature measurements) was obtained by simple mixing of the powder with the solvent to obtain a 10 mg/mL suspension. 3 mL of the suspension was collected for analysis. In the case of deionized water, the suspension was obtained by treating 60 mg of 1:1 MNP/CTAB mixture powder with 3 mL of water to obtain a 10 mg/mL suspension of magnetic nanoparticles. The concentration in both cases was referred to as the weight of MNPs. Finally, all the suspensions were treated in an ultrasound bath for few minutes for better dispersion prior to analysis.

2.2.1. TEM Analysis for Shape and Size

Dried NPs were dispersed in fluid in order to perform the analysis of the morphology with the aim of investigating the shape and the size by means of transmission electron microscopy (TEM), model TECNAI FEI G2 (FEI company, Hillsboro, OR, USA). A drop of well-mixed fluid was deposited on the TEM grid and analyzed at a suitable magnitude. In this case, the NPs were dispersed in octane or hexane. For each sample, at least 10 representative pictures are acquired using the camera of the instrument. These pictures were elaborated by means of the software ImageJ, version 1.53v 21 (public domain Java image processing program developed by NIH, National Institutes of Health, Bethesda, MD,

USA [57]). The nanoparticle shape was identified, and the diameters were measured using the measurement tools. For each sample, a few hundred of nanoparticles were measured, and the average diameter and the corresponding standard deviation were evaluated. The histogram of the diameters was also obtained, and eventually different populations of diameters were identified. In case different sub-populations were identified in the entire population, the average diameter and the frequency of each sub-population were evaluated.

2.2.2. Hydrodynamic Radius

The NPs hydrodynamic diameter was determined by Dynamic light scattering (DLS) measurements using a Malvern Zetasizer 3000HS (Malvern Panalytical, Malvern, UK). All the samples (10 μL of $\text{NP}_{[10 \text{ mg/mL}]}$) were analyzed in 1 mL of water or octane at 25 $^{\circ}\text{C}$ after 15 minutes sonication in an ultrasonic bath [58].

2.2.3. Magnetic Properties

The magnetic properties of the samples were measured using a Quantum Design superconducting quantum interference device (SQUID, Quantum Design Inc., San Diego, CA, USA) magnetometer operating in the 5–300 K temperature range (maximum applied field 50 kOe) [59].

2.2.4. ICP-MS Characterization

The composition of the MNPs in terms of Fe and Mn content was determined by inductively coupled plasma mass spectrometry (ICP-MS) (Element-2; Thermo-Finnigan, Rodano (MI), Italy) at medium mass resolution. Sample digestion was performed with 1 mL of concentrated HNO_3 (70%) using a high-performance Microwave Digestion System (ETHOS UP Milestone, Bergamo, Italy). A natural abundance iron standard solution was analyzed during sample runs in order to check changes in the systematic bias. The calibration curve was obtained using four Fe and Mn absorption standard solutions (Sigma-Aldrich, St. Louis, MO, USA) in the range 0.2–0.01 $\mu\text{g/mL}$ [58].

From the ICP-MS data, the mass of nanoparticles, m_{NP_P} , corresponding to the mass of powder dispersed in the suspension fluid was determined [51,58,59].

2.3. Temperature vs. Time Characterization

2.3.1. Nanofluid Heating

The nanofluids were heated by means of an inductor connected to a generator EASY-HEAT 10.0 kW (manufactured by Ambrell Corporation, Rochester, NY, USA) that generates a time-varying magnetic field at 177 kHz or 245 kHz. The cylindrical inductor in air was formed by 7 turns with an internal diameter of 8 cm. The supply current was varied between 100 A to 500 A which corresponds to a magnetic field between 4.5 to 21.0 kA/m (between 56 and 263 Oe) [60,61]. The temperature of each sample was recorded for different values of magnetic field amplitude and frequency. Temperature measurements were repeated more than three times. The measurement set-up is represented in Figure 1 [61].

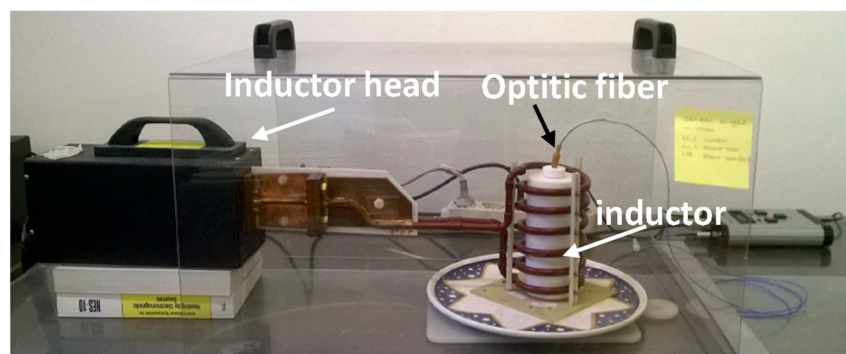


Figure 1. Temperature measurement set-up.

For experimental tests, a sample of 3 mL of the nanofluid, at 10 mg/mL in NP powder, was placed in a 5 mL test tube. The test tube was placed in a holed Teflon cylinder, with an external diameter of 7 cm and an internal hole with diameter of 3 cm, equipped with a threaded cap where the test tube, with a diameter of 1 cm, can be screwed. This way a layer of air is interposed between the test tube and the Teflon cylinder. The cap was equipped with a hole for the temperature sensor. The aim of the cylinder is to maintain the adiabatic conditions in the first few minutes of the heating process. The nanofluid temperature in a predefined time interval was recorded using a fiber optic thermometer Fo-temp (manufactured by Optocom, Stendal, Germany).

Time-temperature data were collected and used to evaluate the SLP by means of three different methods. In the considered samples in a preliminary experiment, we evidenced that the temperature increment of the fluid due to the induced current in the suspension fluid was negligible. Moreover, in our measurement system, the vial with the sample was placed in a hole cylinder with an air layer 2 cm thick. This way the temperature inside the sample was less influenced by external temperature. Then, the temperature data were used as collected.

2.3.2. SLP Obtained by Exponential Function Analysis

In case of the temperature of the nanofluid recorded in a time interval 2400 s long, the SLP was evaluated as in [43,44]. In this case, the temperature versus the time shows an exponential behavior where the temperature evolution in the time $T(t)$ is, can be described by means of the exponential function typical of heating phenomena based on the maximum temperature gap between the initial time step and the temperature at the steady state condition considered the final time step, ΔT_{max} as described by Andreu and Natividad in [44]:

$$T(t) = T_0 + \Delta T_{max} \left(1 - e^{-\frac{t}{\tau}}\right) \tag{1}$$

where T_0 is the initial temperature at the time step 0 s, t is the time and τ is the time constant of the exponential function that represents the heating process as evidenced in Figure 2. From the initial slope, the SLP was evaluated in a time interval lower than half of the time constant.

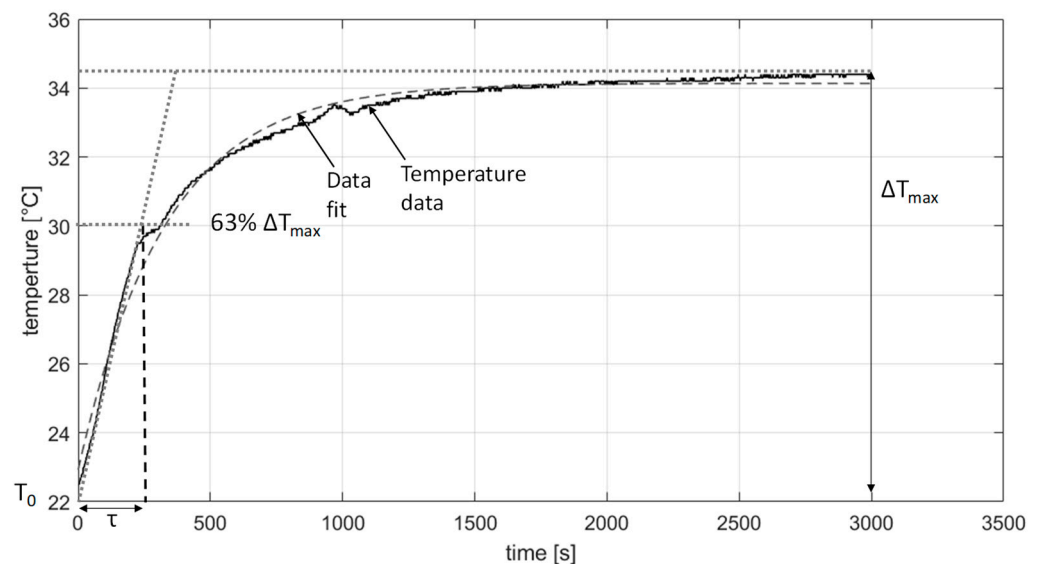


Figure 2. Temperature data as a function of time for measured temperature (continuous line) and fitted curve (dotted line). Identification of the parameters in the curve of Equation (1).

Fitting the time-temperature curve by means of the minimum least squares method using Matlab fitting tool the values of T_0 , ΔT_{max} and τ were evaluated. Given the fitting parameters of Equation (1), according to [44], the SLP could be evaluated as:

$$SLP(A) = \frac{C}{m_{MNP}} \cdot \frac{\Delta T_{max}}{\tau} \quad (2)$$

where m_{MNP} is the mass of NPs, ΔT_{max} and τ were the maximum temperature gap and the time constant of the heating curve, respectively, and C , in [J K^{-1}], is the heat capacity of the suspensions approximated to the specific heat of the fluid ($4.18 \text{ [J g}^{-1} \text{ K}^{-1}]$ for water and $2.238 \text{ [J g}^{-1} \text{ K}^{-1}]$ for octane) multiplied by the mass of the fluid. In fact, the contribution of the heat capacity of the mass of dispersed NPs is negligible with respect to that of the fluid alone and is approximated by that of the fluid as in [9] since the contribution of the MNPs to the C constant, evaluated as in [44], is less than 1% (considering a specific heat for magnetite close to $0.67 \text{ [J g}^{-1} \text{ K}^{-1}]$ [7] and NPs mass of 10 mg). The values ΔT_{max} and τ were evaluated fitting the temperature curve.

The SLP evaluated as in Equation (2) was computed considering the frequency of 177 kHz and considering the peak of the magnetic field at 170 Oe.

2.3.3. SLP Obtained by Initial Slope Method

The SLP could be computed also considering the initial slope of the temperature curve evaluated by means of the ratio between the temperature increment, $\Delta T(\Delta t)$, evaluated in a time interval, Δt , with $\Delta t = 60 \text{ s}$ [43,44]:

$$SLP(B) = \frac{C}{m_{MNP}} \cdot \frac{\Delta T(\Delta t)}{\Delta t} \quad (3)$$

In this evaluation, the first 10 s of the temperature curve were discarded. In this method, the quasi-adiabatic interval has to be identified. In particular, other authors evaluate the slope of the temperature rise in different intervals discarding the first 10 s of the temperature curve. The intervals 20 s, 30 s, 60 s, and 90 s were considered and the temperature vs. time slope was computed. Homogeneous values of slope identify linear heating that corresponds to a quasi-adiabatic condition [44,45,48]. In the examined cases the interval $\Delta t = 60 \text{ s}$ fit with all the samples examined.

2.3.4. SLP Obtained by Quasi-Adiabatic Calculation

The temperature of the nanofluid was recorded in a time interval of 160 s long (150 s AMF ON and 10 s AMF OFF). The SLP related to the nanofluid was evaluated as in [48]. Briefly, before turning the AMF power ON, temperature of the IONP colloid was monitored for a few minutes to ensure the temperature was stable (variation $\leq 0.1 \text{ }^\circ\text{C}$) and the colloid was in thermal equilibrium with the environment. Next, the AMF power was turned ON and temperature was recorded for 160 s. Temperature vs. time was also recorded for water blanks for the same AMF settings (H, f). This measurement was performed three times the first day of the experiment. From this data, excluding the first 10 s from analysis and considering the value until 110 s, the net temperature increase, and incremental temperature increase were calculated for IONP colloids. The net temperature increase of the samples was calculated by subtracting the temperature collected in the first sample at time 0 s. Next, the heating rate, evaluated as the slope of the net temperature increase curve in predefined time intervals, e.g., between 10 and 60 s or between 10 and 110 s, which satisfied quasi-adiabatic conditions [33,35], was used to calculate SLP using methods previously described and will be labeled as QA-SLP method, Quasi Adiabatic-SLP [45,48]. In the considered measurement set-up, the interval 10–60 s is approximately adiabatic.

The SLP values were computed considering the NP total mass (10 mg/mL) for a volume of 3 mL of water or octane.

The SLP using adiabatic method was evaluated at 177, 215, and 245 kHz and considering different magnetic field intensities with peak-to-peak between 113 and 263 Oe (9 to 21 kA/m, peak value).

3. Results

3.1. Magneto-Fluid Characterization

3.1.1. Size Analysis from TEM Image

The TEM images of the analyzed nanoparticles and the histogram of the diameter distributions were reported in Figure 3. The shape of the nanoparticles is approximately cube-shaped for sample C26, irregular with round and triangular elements for C12, and irregular with approximately sphere-shaped for the C5 sample. The average diameter of the magnetic core of the nanoparticles was measured and reported in Table 1. The Anderson-Darling test verifies that the null hypothesis (the distribution of the diameters of the nanoparticles is normal) is not true (p -value < 0.005) for all the samples considered. Only for sample C12 is a Lognormal distribution (p -value = 0.2) identified.

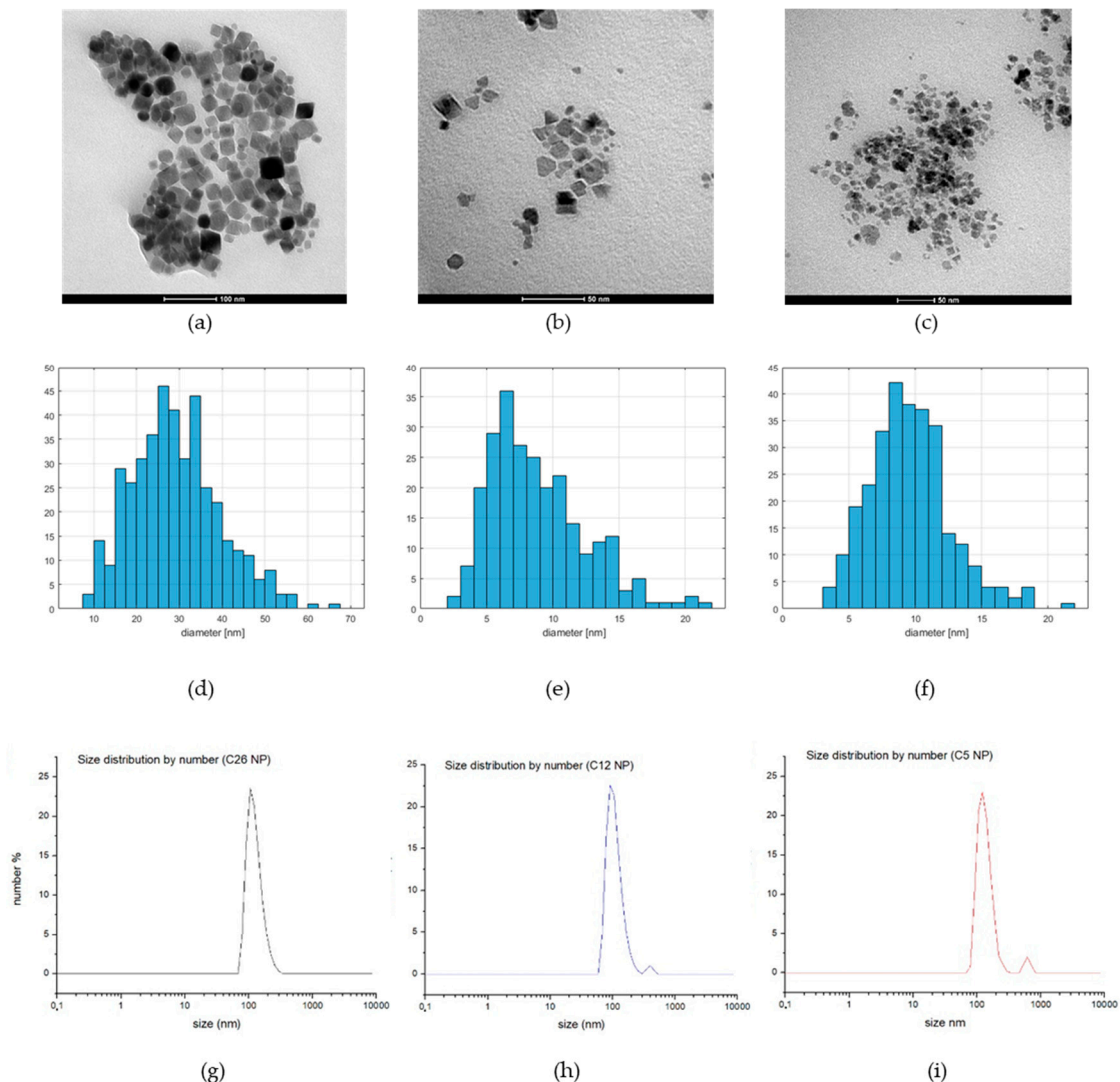


Figure 3. (a–c) TEM of the nanoparticles, (d–f) the histograms of the diameter, and (g–i) representative size distribution profile by number measured by Dynamic Light Scattering: (a,d,g) Iron-Mn sample, C26, (b,e,h) thermal decomposition Iron-Oxide sample, C12, (c,f,i) coprecipitation Iron-Oxide sample, C5.

Table 1. NP size in terms of magnetic core and hydrodynamic diameter (water suspension). * The hydrodynamic mean diameter was obtained by the number-weighted distributions that represent the number of molecules in each bin in a given histogram, derived from the intensity distribution using the Mie theory [62,63]. Std = standard deviation, PDI = polydispersity index.

	Magnetic Core Diameter		Hydrodynamic Diameter *		
	Average [nm]	Std [nm]	Average [nm]	Std [nm]	PDI
C26	29.2	±10.2	109(100%)	±8	0.43
C12	8.8	±3.7	132(97%) 486 (3%)	±15 ±94	0.51
C5	9.5	±3.1	132 (95%) 610 (5%)	±28 ±198	0.46

3.1.2. Size Analysis: Hydrodynamic Diameter

Table 1 also shows the hydrodynamic diameter of the nanoparticles which also include the non-metallic external shell. The mean diameter was obtained by the number-weighted distributions that represent the number of molecules in each bin in a given histogram (as in Figure 3h–l, derived from the intensity distribution using the Mie theory [62,63]. From the hydrodynamic and magnetic diameters, the thickness of the external shell was evaluated in the case of NP dispersed in octane. The hydrodynamic and magnetic diameters for the NPs in water are related to the size of the NP aggregate.

3.1.3. Magnetic Properties

The magnetic loops measured at temperatures $T = 5\text{ K}$ and 300 K are shown in Figure 4. The magnetization has been obtained by dividing the magnetic moment, measured by SQUID, by the mass of the MNPs alone (i.e., excluding the oleate).

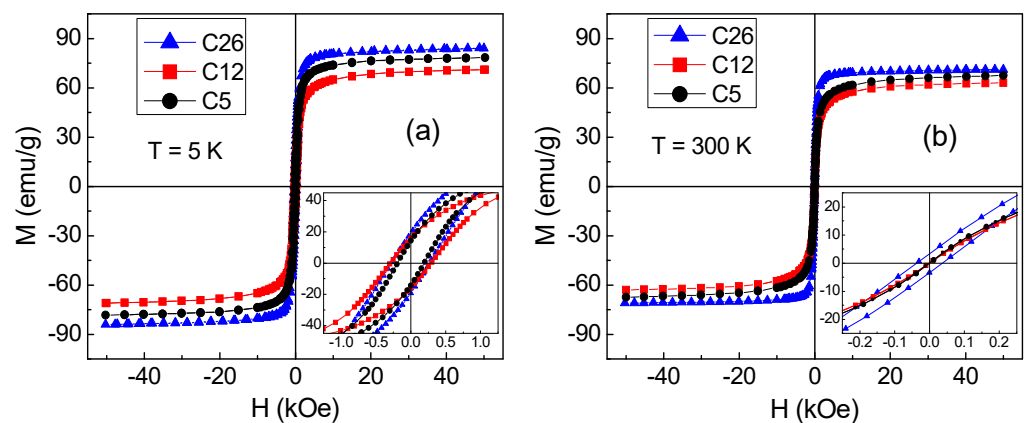


Figure 4. Magnetic loops measured on the three samples at $T = 5\text{ K}$ (a) and $T = 300\text{ K}$ (b). The insets are zoomed views of the central region of the loops.

Magnetite has an inverse spinel structure in which the trivalent ions Fe^{3+} (bearing a magnetic moment of $5\ \mu_B$) are equally distributed in the tetrahedral (A) and octahedral (B) sites and the divalent ions Fe^{2+} (magnetic moment of $4\ \mu_B$) are placed in the B sites, as expressed by the notation $[\text{Fe}^{3+}]_A[\text{Fe}^{2+}\ \text{Fe}^{3+}]_B\text{O}_4$. A net magnetic moment is provided by the Fe^{2+} ions since those associated with the Fe^{3+} ions annihilate reciprocally, being the superexchange interaction between A and B sites antiferromagnetic in nature. Hence, the predicted magnetic moment per unit cell is $4\ \mu_B$ and the expected value of saturation magnetization at $T = 5\text{ K}$ is $M_s \sim 98\text{ emu/g}$ [64].

However, a lower M_s is measured on the investigated samples at $T = 5\text{ K}$ (Table 2). In particular, M_s decreases with decreasing the mean size of the MNPs (Table 1). This is a finite-size effect often reported for ferrite MNPs and ascribed to the spin canting

phenomenon, i.e., a lack of spin collinearity in the spinel structure. The effect of spin canting is strictly associated with the presence of structural disorder, therefore low crystallinity, at the surface and/or in the core of the MNPs. In fact, it is due to reduced and modified atomic coordination and the presence of topological defects, resulting in altered super-exchange bonds [59,65–68].

Table 2. Magnetization at different temperatures.

	M_S at T = 5 K (emu/g) $\pm 2\%$	M_S at T = 300 K (emu/g) $\pm 2\%$
C26	86	72
C12	73	65
C5	80	69

The highest M_S (~86 emu/g) is measured in C26 MNPs. This is consistent with the fact that they have the largest mean size and quite a regular cubic shape. The latter feature has been shown to imply a higher degree of crystallinity, compared to the spherical shape [69,70]. Moreover, in Mn-doped magnetite, which is the case of this type of MNP, the possible substitution of Fe^{2+} ions with Mn^{2+} ions (isoelectronic with Fe^{3+} and hence with a magnetic moment of $5 \mu_B$) brings about an increase of the magnetic moment per unit cell and therefore of the saturation magnetization [71–73].

In all the samples the coercivity H_C is in the 200–300 Oe range at T = 5 K; at T = 300 K, $H_C \sim 36$ Oe in C26 whereas the absence of magnetic hysteresis (i.e., null coercivity and remanent magnetization) in C12 and C5 is in favor of a superparamagnetic behavior of the whole MNPs assemblies.

In fact, it is well known that MNP can exhibit magnetization relaxation, possibly culminating in the superparamagnetic behavior when the thermal energy is comparable to the anisotropy energy barrier for the reversal of its magnetic moment [74].

The blocking temperature T_B above in which an isolated single-domain MNP enters the superparamagnetic regime is expressed by the relation:

$$T_B = \frac{KV}{k_B \ln(t_m f_0)} \quad (4)$$

where KV is the magnetic anisotropy energy barrier (K anisotropy coefficient, V volume of the MNP), k_B is the Boltzmann constant, t_m is the measuring time characteristic of the used investigating technique, and f_0 is a frequency factor [74]. A value of $\ln(t_m f_0) \sim 25$ is usually considered for SQUID measurements, which assumes $t_m = 100$ s and $f_0 = 10^9$ s⁻¹ [71,75].

To gain more information in this respect, we have performed magnetization measurements as a function of increasing temperature (heating rate 3 K/min) in a static magnetic field $H_{\text{appl}} = 50$ Oe, after cooling the sample from room temperature down to T = 5 K without (zero-field-cooling, ZFC) and with H_{appl} (field-cooling, FC). The results for the three samples are shown in Figure 5. The magnetic irreversibility effect (difference between the values of M_{FC} and M_{ZFC}) is consistent with the relaxation processes of the magnetic moments of the MNPs.

In an assembly of size-distributed MNPs, a distribution of T_B also exists. If the MNPs can be assumed as non-interacting, M_{ZFC} is expected to show a peak at a temperature T_{max} that represents an average blocking temperature and can be estimated from Equation (4), considering the mean volume of the assembly; the M_{FC} branch is expected to decrease with increasing T and to collapse on M_{ZFC} at a temperature T_{irr} , corresponding to the blocking temperature of the largest MNPs of the assembly [74].

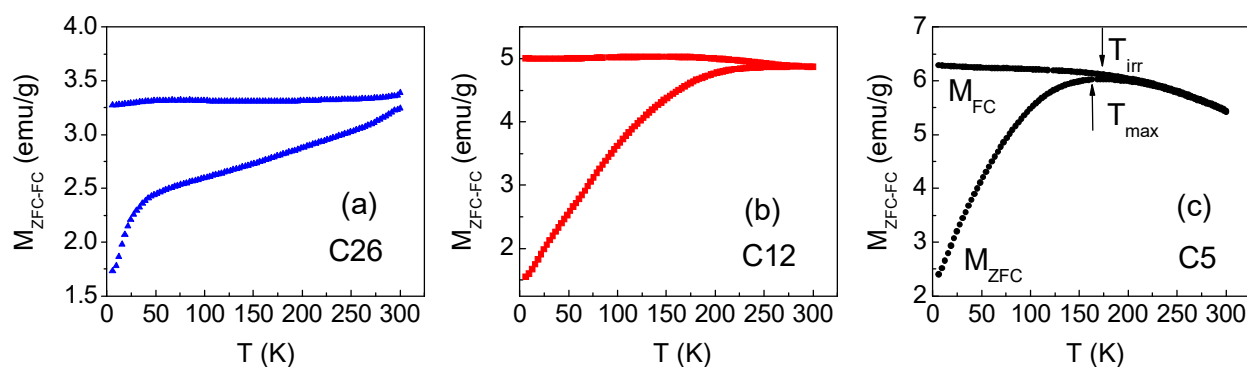


Figure 5. Magnetization measured in ZFC mode (MZFC, lower branches) and FC mode (MFC, upper branches) for increasing temperature (T), in $H_{\text{appl}} = 50$ Oe, on samples C26 (a), C12 (b), and C5 (c).

Thus, for C5 and C12 MNPs, having a mean size around 10 nm (even less, Table 1), setting K equal to that of bulk magnetite (1.1×10^5 erg/cm³) gives an average blocking temperature of ~ 20 K. However, the temperature T_{max} , at which M_{ZFC} reaches a sort of very broad peak, is definitely higher (Figure 5b,c; as an example, T_{max} and T_{irr} are indicated for C5). This is to be ascribed mainly to magnetic dipolar interactions between the MNPs, which result in an increase of their effective anisotropy energy barriers [41,71,74–81].

Other features revealing that interparticle dipolar interactions affect the magnetic relaxation of the nanoparticles are: (i) the trend of M_{FC} , which tends to become constant below T_{max} ; (ii) the observation that, in spite of the wide size distribution of the C12 and C5 MNPs (Figure 3f,g), T_{irr} is very close to T_{max} because magnetic interactions act so as to narrow the distribution of effective anisotropy energy barriers, being the relaxation of the MNPs no longer fully independent [74]. However, Figure 5b,c confirm that the C5 and C12 MNPs are in the full superparamagnetic state at $T = 300$ K, in agreement with the null values of coercivity and remanent magnetization (inset of Figure 4b).

The relaxing behavior of the C26 MNPs appears more complex. The M_{ZFC} and M_{FC} branches are not seen to merge even at $T = 300$ K, which indicates that the superparamagnetic state of the whole MNPs assembly is not achieved under the adopted experimental conditions, in line with the fact that H_{C} does not annihilate (inset of Figure 4b). This indicates that higher anisotropy energy barriers are associated with the C26 MNPs, compared to C5 and C12, certainly due to their larger mean size and wide size distribution, good crystallinity, and stronger dipolar interactions also by virtue of the higher M_{S} . In this last respect, the abrupt decrease of M_{ZFC} below ~ 40 K is reminiscent of a long-range collective freezing of the MNPs magnetic moments under the action of dipolar interactions, probably involving the smaller MNPs of the assembly [82–84]. Above $T \sim 40$ K, the linear rising trend of M_{ZFC} , typical of a ferromagnet, confirms the presence of non-relaxing MNPs, which coexist with the fraction of relaxing ones.

3.1.4. ICP-MS Analysis

Table 3 reports the Iron and Manganese content measured in a sample of 10 mg in weight of NP powder using ICP-MS.

Table 3. Iron and Manganese content evaluated on a sample of 10 mg of NP powder and the mass of the metallic oxide. ICP-MS method.

	Fe Fe/10 mg NP [mg]	Mn Mn/10 mg NP [mg]	Fe ₃ O ₄ /10 mg NP [mg]	Mn _x Fe _{3-x} O ₄ /10 mg NP [mg]
C26	5.54 ± 0.28	0.86 ± 0.04	-	8.85
C12	5.76 ± 0.29	-	7.96	-
C5	7.07 ± 0.35	-	9.77	-

The mass of magnetic core material in the samples based on ICP-MS analysis (Table 3) is based on the magnetite formula (Fe_3O_4) for samples C12 and C5, while for C26 has been determined on the hypothesis of a Mn-doped ferrite spinel of general formula $\text{Mn}_x\text{Fe}_{3-x}\text{O}_4$. Based on the experimental Mn/Fe ratio an average formula of $\text{Mn}_{0.41}\text{Fe}_{2.59}\text{O}_4$ can be proposed, in agreement with our previous findings [71]. In the NPs obtained by thermal decomposition (C26 and C12), the relative amount of stabilizing agent (oleate w% = 11.5% and 20.4%, respectively) is higher than that in the coprecipitated ones (C5 with 2.3%), suggesting a more efficient surface functionalization in the treatment at high temperature.

3.2. Temperature vs. TIME Characterization

3.2.1. Evaluation of the SLP by Means of the Exponential Method and Initial Slope

Figure 6 shows an example of a typically normalized temperature increment as a function of the time related to the different nanofluids analyzed at a given frequency and magnetic field intensity. Table 4 reports the SLP evaluated by means of the three computation methods expressed by Equations (1) and (2) and QA-SLP for three different temperature-time curves. The temperature was recorded on a time interval of 2400 s applying a magnetic field at 177 kHz with a maximum value of 170 Oe. All the curves reach the limit temperature at a steady state. The measurements were repeated three times and the average SLP was computed for each NP sample. The temperature values were normalized to the initial temperature then Figure 6 represents the temperature increment with respect to the initial temperature.

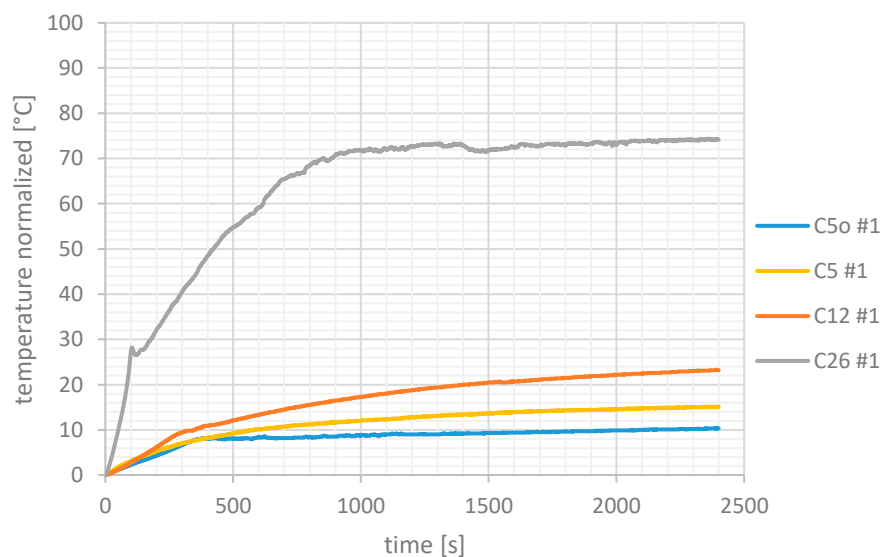


Figure 6. Example of the temperature-time curve recorded for 2400 s applying to the magnetic fluid a sinusoidal magnetic field at 177 kHz with maximum value 170 Oe. Values normalized to the initial temperature.

Figure 6 shows an example of a typically normalized temperature increment as a function of the time related to the different nanofluids analyzed at a given frequency and magnetic field intensity. The temperature was acquired up to 2400 s (40 min) and in this acquisition interval, it arrives at a T_{\max} value. At around 100 s, the C26 curve experiments with a modification of the slope in the heating curve, and a small peak is visible. This could be due to the deposition of the fluid in the bottom of the vial. Then only half of the first-time interval, (up to 100–120 s) could be used to evaluate SLP using the slope method. Consequently, for this sample, an interval of 60 s could be adequate to evaluate SLP. This phenomenon was less visible for the C5 and C12 nanofluid samples at around 300–400 s. The observation of the behavior of curves in Figure 6 and the determination of the approximated time constant of the exponential suggested the amplitude of the quasi-adiabatic interval characteristic of each nanofluid. Table 4 reports the SLP evaluated

by means of the three computation methods expressed by Equations (1) and (2) and QA-SLP for three different temperature-time curves. The temperature was recorded on a time interval of 2400 s applying a magnetic field at 177 kHz with a maximum value of 170 Oe. All the curves reach the limit temperature at a steady state. The measurements were repeated three times and the average SLP was computed for each NP sample. The temperature values were normalized to the initial temperature then Figure 6 represents the temperature increment with respect to the initial temperature.

Table 4. SLP value evaluated applying the three methods, SLP(A), i.e., exponential method, SLP(B), i.e., Initial slope method, and QA-SLP, i.e., Quasi-Adiabatic method, to the long-time data (three series) and average value for a sinusoidal magnetic field with maximum value 170 Oe at 177 kHz. Samples with volume 30 mL with 10 mg/mL of NP powder.

NP	C5o#1 *	C5o#2 *	C5o#3 *	Average	C5#1	C5#2	C5#3	Average
SLP (A) [W/g]	5.41	5.85	4.85	5.37 ± 0.50	8.35	9.54	9.07	8.99 ± 0.60
SLP (B) [W/g]	3.69	4.48	3.95	4.04 ± 0.40	13.26	12.56	13.26	13.03 ± 0.40
QA-SLP [W/g]	3.80	4.52	3.79	4.04 ± 0.42	14.50	12.57	13.17	13.42 ± 0.99
σ (QA-SLP) [W/g]	0.13	0.10	0.28	0.11	0.38	0.28	0.37	0.20
NP	C12#1	C12#2	C12#3	Average	C26#1	C26#2	C26#3	average
SLP (A) [W/g]	12.87	11.33	9.58	11.26 ± 1.65	84.44	75.68	59.19	73.10 ± 12.82
SLP (B) [W/g]	11.16	13.26	14.65	13.03 ± 1.75	96.25	106.01	101.83	101.37 ± 4.90
QA-SLP [W/g]	11.56	13.85	14.50	13.30 ± 1.54	97.50	106.43	104.21	102.71 ± 4.65
σ (QA-SLP) [W/g]	0.77	0.64	0.70	0.41	4.85	0.95	1.88	1.76

* o subscript indicates an octane.

The different NP samples show different temperature-time curves. In particular, pure Iron-oxide NPs show a smaller temperature increment with respect to the Mn-Iron-oxide sample. The heating properties of the different samples were evaluated by means of the SLP computed on the mass of NP dispersed in 3 mL of fluid. Then considering a NP powder concentration of 10 mg/mL, the SLP values using the initial slope method and the QA-SLP were computed considering a time interval between 10 and 60 s. In the interval of 10–60 s, the quasi-adiabatic condition is verified considering the criterion described in the Methods paragraph. Data in Figure 6 suggest the length of time analysis depends on the initial temperature rate: the faster the temperature increment, the shorter the analysis window. For instance, the C26 nanofluid has a heating rate of 10 °C in less than 40 s, whereas the other nanofluids show a 10 °C gap in 300 s. The behavior of the time curve in Figure 6 related to sample C26 suggests the presence of two time constants of the heating phenomena related to a first faster slope followed by a slower slope after the peak. This peak that occurs around 200 s represents the time instant at which the nanoparticles were deposited on the vial bottom. In fact, after 1 min the nanoparticles appear deposited on the vial bottom and they are separated by suspension fluid. This way two phases are in the vial: a small volume with all the nanoparticles and the fluid. The first part of the curve represents the heating of the fluid when the nanoparticles were homogeneously distributed in the fluid and the part after the small peak represents the fluid heating by the heating source, the nanoparticles, deposited on the vial bottom. Then, the phase separation that occurs in sample C26 suggests the need to set the time length of the window analysis shorter than the other nanofluids that did not experience the phase separation. For the other sample, a different time window could be considered and a typical length is between 60 and 100 s. From Table 4 it appears that the SLP(B) and QA-SLP methods give equivalent results. The advantage of QA-SLP methods is that the analysis window is not predetermined but is sized according to data.

Figures 7 and 8 show the SLP histogram evaluated using QA-SLP and the temperature as a function of the time in the measurement interval between 0 and 160 s for the samples C5 (Figure 7A,B), C12 (Figure 7C,D), and C26 (Figure 8C,D). All the samples were dispersed in water, and they are heated by applying a magnetic field of 227 Oe at 5 kHz. Figure 8A,B refer to sample C26 where the water dispersed when the time-varying magnetic field amplitude is 170 Oe. In particular, the data in panels (C,D) in Figure 8 related to sample C26 show a double slope. After 120 s and 80 s sample experiences, first, faster heating was followed by a temperature decrement and a different slope of the temperature as a function of time. The new temperature slope is lower with respect to the one at the magnetic field turn-on. In fact, in this time interval, NPs deposited on the vial bottom, then the suspension fluid heating is related to a heating source (NPs) more concentrated than by heating the fluid by convection.

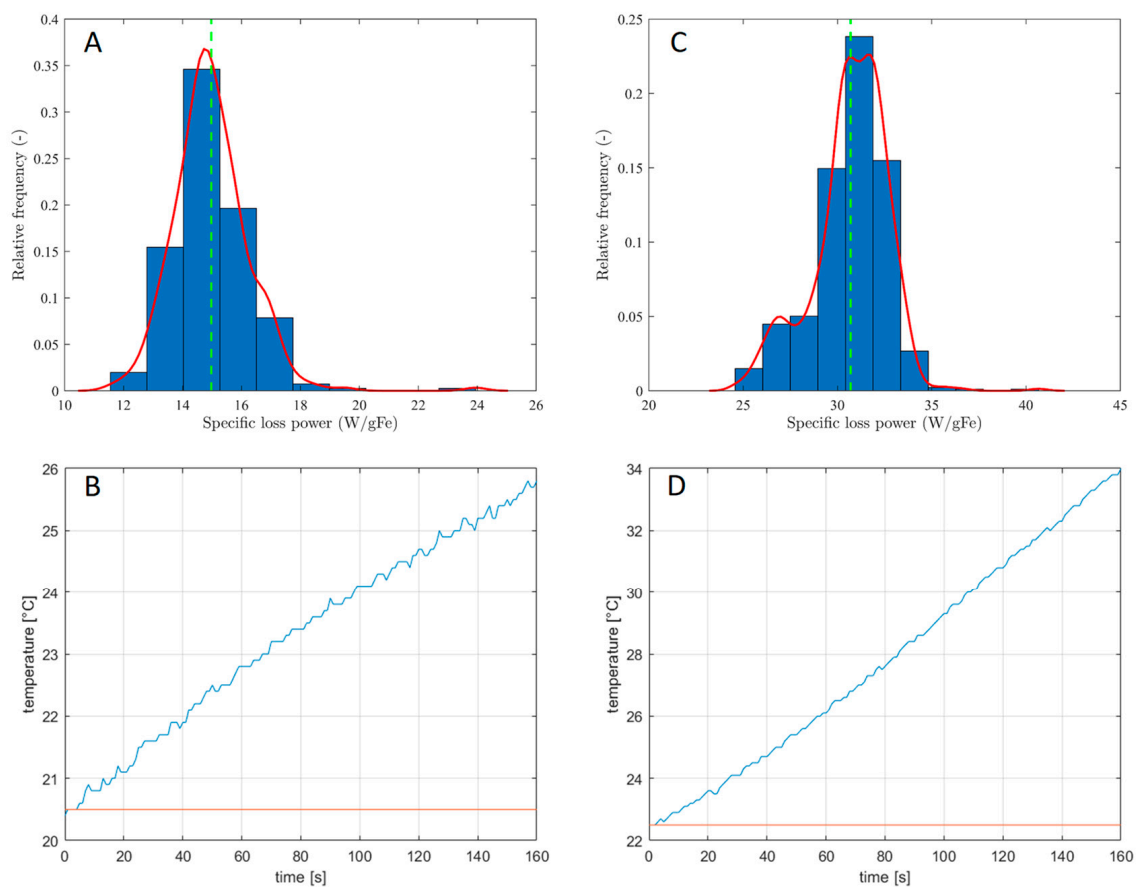


Figure 7. Histogram of the SLP values evaluated in a 10–100 s time interval and corresponding temperature measured in an acquisition 160 s long. (A,B) sample C5, and (C,D) sample C12 dispersed in water. Applied magnetic field at 177 kHz with magnitude 227 Oe.

The p -values obtained from ANOVA analysis (see Table 5) suggest that the QA-SLP and SLP (B) methods provide similar results in terms of SLP values (p -value > 0.05), while SLP (A) provides different results with the exception of sample C12.

Iron oxide NPs (C12 and C5) have SLP histograms that show a symmetric distribution around an average value, whereas the histogram of SLP of C26 NPs shows a non-symmetric distribution. The non-symmetric distribution shows a modification of the SLP during the first second of heating, whereas the symmetric distribution identifies a constant SLP.

Table 5. *p*-value related to ANOVA analysis to compare two by two of the SLP evaluated using the three methods, SLP(A), i.e., exponential method, SLP(B), i.e., Initial slope method, and QA-SLP, i.e., Quasi-Adiabatic method, for the data series in Table 4.

	C5o *	C5	C12	C26
SLP (A)-SLP (B)	0.0231	6.37×10^{-4}	0.2734	0.0234
SLP (B)-QA-SLP	0.9925	0.5643	0.8459	0.7466
SLP (A)-QA-SLP	0.0241	0.0027	0.1920	0.0198

* o subscript indicates an octane.

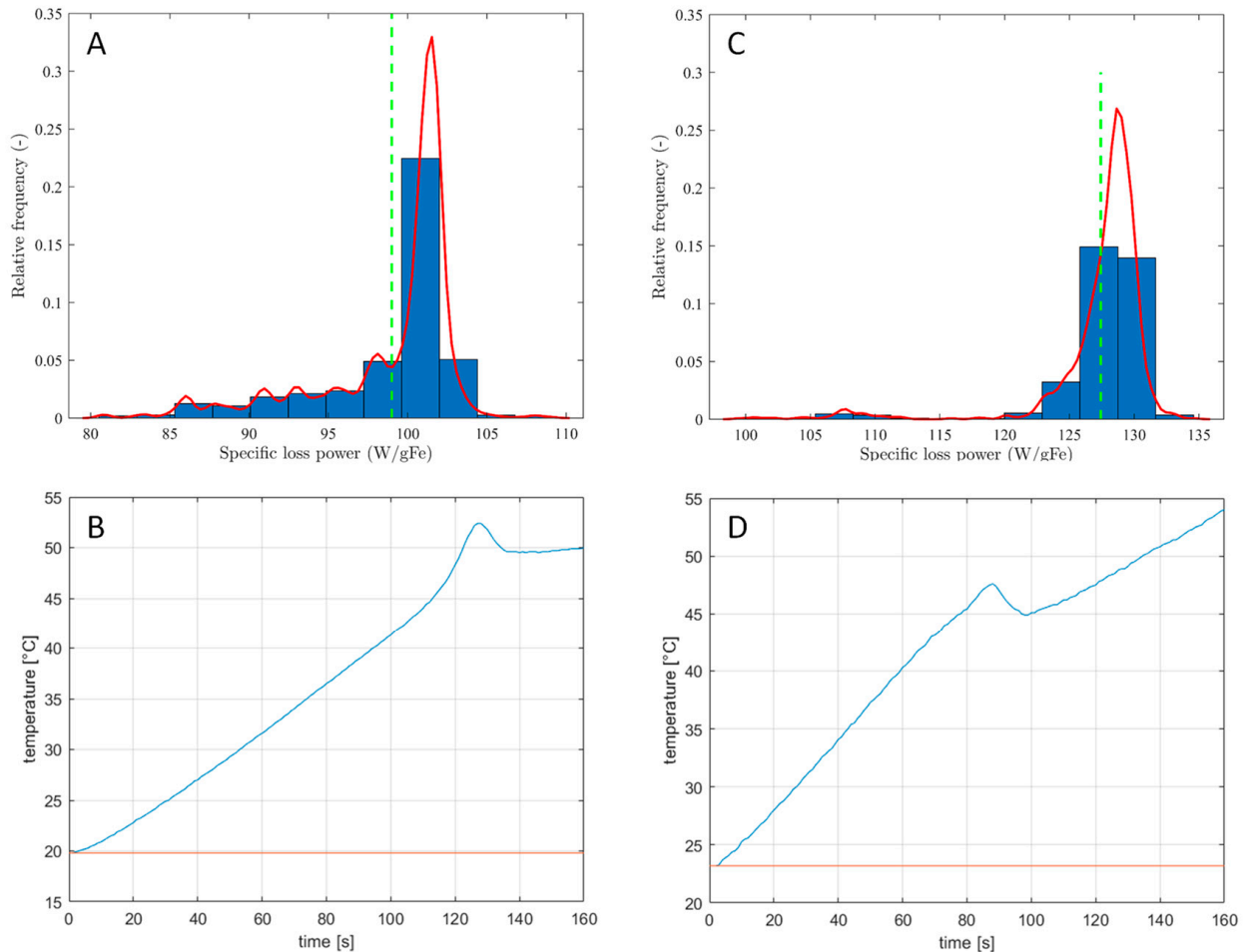


Figure 8. Histogram of the SLP values evaluated in a 10–100 s time interval and corresponding temperature measured in an acquisition 160 s long. Value for the sample Iron-Mn sample, C26, water dispersed considering a magnetic field (A,B) at 177 kHz with magnitude 170 Oe, and (C,D) at 177 kHz with magnitude 227 Oe.

3.2.2. Evaluation of the SLP by Selection of Quasi-Adiabatic Heating Interval

Table 6 and Figure 9 report the average SLP values (evaluated using three measurements of the same sample), with the standard deviation of the average, computed using the software developed by [45]. The SLP was evaluated on a time range between 10 and 100 s from the start of the temperature recording as in [45]. The temperature curves were recorded for different magnetic field intensity values at three different frequencies.

Table 6. SLP value and related standard deviation evaluated applying the quasi-adiabatic methods (average value of three series) for different magnetic field intensities at three different frequencies. Linear fit for a right with 0-intercept and its R2 value.

f [kHz]	Field [Oe]	C5 Octane		C5 Water		C12 Water		C26 Water	
		SLP [W/gNP]	σ (SLP)						
177	113	1.99	0.09	5.19	0.39	3.52	0.12	33.27	0.73
177	170	4.36	0.73	12.85	0.31	12.67	1.01	102.43	1.48
177	227	5.86	0.24	14.92	0.21	31.24	0.59	132.89	6.15
Linear fit		0.066 ($R^2 = 0.981$)		0.025 ($R^2 = 0.987$)		0.104 ($R^2 = 0.868$)		0.551 ($R^2 = 0.967$)	
215	113	3.37	0.12	8.62	0.17	5.19	0.18	42.30	3.02
215	132	4.67	0.19	10.6	0.24	8.39	0.44	73.98	0.86
215	263	7.85	0.72	16.82	0.31	46.83	0.24	192.81	3.87
Linear fit		0.068 ($R^2 = 0.99$)		0.031 ($R^2 = 0.99$)		0.141 ($R^2 = 0.863$)		0.657 ($R^2 = 0.965$)	
245	56	2.33	0.86	3.22	0.37	1.73	0.12	2.28	0.21
245	113	3.52	0.12	10.62	0.52	5.59	0.16	44.22	0.64
245	170	6.14	0.22	15.38	0.35	17.65	1.05	126.76	2.46
Linear fit		0.089 ($R^2 = 0.99$)		0.035 ($R^2 = 0.99$)		0.088 ($R^2 = 0.898$)		0.595 ($R^2 = 0.88$)	

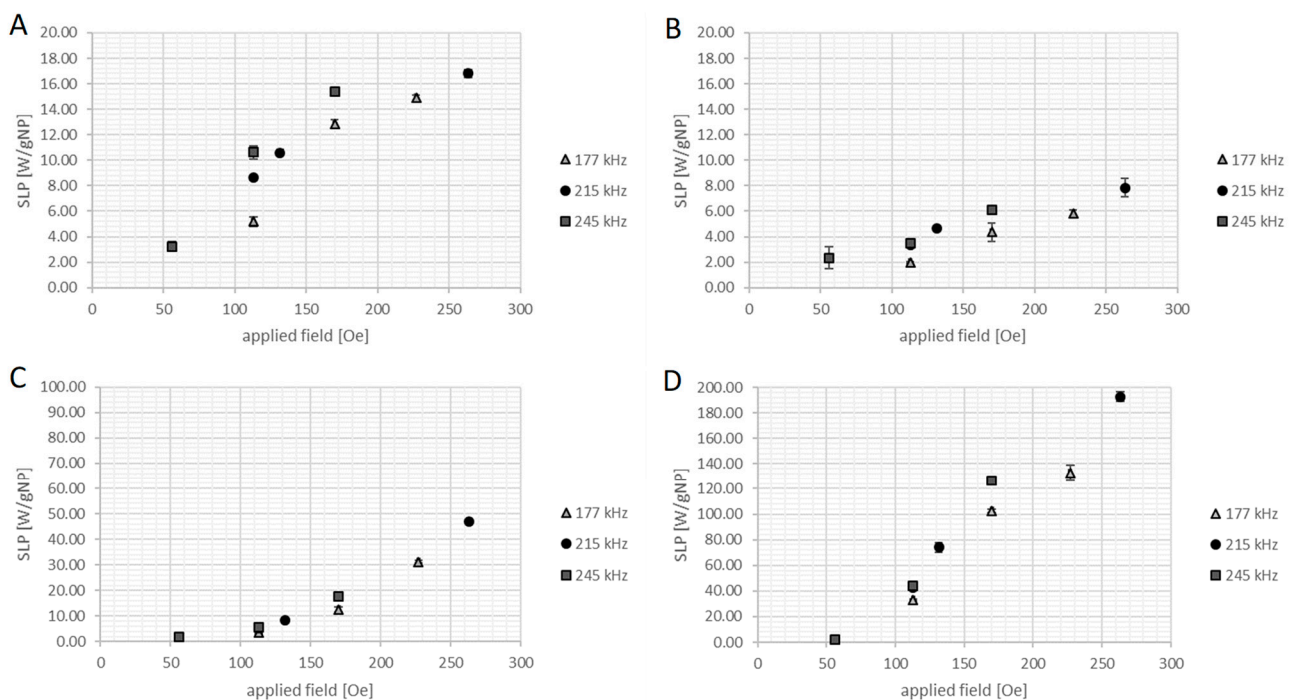


Figure 9. Average SLP value evaluated applying the quasi-adiabatic methods for different magnetic field intensities at three different frequencies: (A) sample C5 dispersed in octane, (B) sample C5 dispersed in water, (C) sample C12 dispersed in water, and (D) sample C26 dispersed in water.

From the analysis of SLP, it is evident that different types of nanoparticles in the same fluid, water, are able to generate different power densities. Moreover, the generated power is different considering different suspension fluids with different heat capacities.

For each series of data at a given frequency of the magnetic field, the points at different magnetic field intensities were fitted with a right line with 0-intercept (no field—no temperature increment), and the slope coefficient of the right line was reported in Table 7 including the R^2 coefficient of the goodness of fit.

Table 7. Comparison of the advantages and disadvantages of the methods for SLP determination.

Method	Advantages	Disadvantages
SLP(A)	<ul style="list-style-type: none"> • Use of theoretical heating curve • Inaccuracy is larger for short measuring times [85] 	<ul style="list-style-type: none"> • Long measurement time (>60 min) • Dependence on the thermal insulation (adiabaticity)
SLP(B)	<ul style="list-style-type: none"> • Short measurement time (≈ 1 min) • Easy to compute 	<ul style="list-style-type: none"> • Uncertainty on the starting point • Possible dependence on the measurement time interval • Averages adiabatic and non-adiabatic portions of the T vs. t curve
QA-SLP	<ul style="list-style-type: none"> • Short measurement time (≈ 1 min) • Dependence on the time interval considered • More consistent with the definition of SLP which assumes an adiabatic precondition to estimation through calorimetry 	<ul style="list-style-type: none"> • Elaborate computation

4. Discussion

4.1. Size Characterization

The magnetic diameters of the NP in the different nanofluids (Figure 3) are dispersed in size as evidenced by the histograms in Figure 3B. The shape is close to a square shape for C26; whereas the other two samples show an irregular shape that could be approximated with a round shape. In sample C12, some big triangular elements or hexagonal elements could be evidenced. The distribution of diameters is not symmetric and normal, but it is an asymmetric distribution that in one case fits with Lognormal distribution since there is a prevalence of smaller particles and big particles are less in number.

The hydrodynamic radius relative to the NPs dispersed in water corresponds to the size of the NP aggregate and any information about the thickness of the non-metallic cover layer can be deducted. Nevertheless, the large hydrodynamic radius confirms the NP organization in macroscopic aggregate when dispersed in water even if they are treated with CTAB.

4.2. Thermal Characterization

From the data in Table 4, it appears that different methods to evaluate the SLP of the same sample can give distinctly different values. The method that uses the initial slope evaluated on the first 60 s of the temperature-time curve, SLP(B), is comparable to the SLP obtained using the QA-SLP that averages the SLP values evaluated by means of slope on different time windows on the time interval (10,100) s. Instead, the method of the fit of the exponential model, SLP(A), shows very different SLP values except for the C12 sample. In general, the SLP value evaluated using the fit of the exponential model [43], SLP(A), shows lower values with respect to the ones obtained with the slope-based methods, except for the sample C5 dispersed in octane for which the SLP(A) is higher with respect to the ones obtained with slope-based methods. From the data in Table 4 it appears that the analysis of the thermal transient using the fit of the exponential model proposed by [43,44] can overestimate or underestimate the NP-SLP, and their values depend on the system in the not-adiabatic segment. The variation of the SLP could be due to the fact that the method, even considering the changes due to loss of adiabatic condition and the thermal exchange with the environment, does not consider the possible structural changes in the sample that may happen in such a long acquisition time. In fact, with sample C26 after a few minutes,

the NPs tended to aggregate and deposit at the bottom of the test tube as confirmed by the small peak at 85–130 s (Figure 6) that appears in the temperature curve corresponding to the liquid-solid separation.

This analysis also allowed us to compare operatively, the advantages and disadvantages of the three methods, as summarized in Table 7.

Finally, the available methods to quantify the magnetic material in the fluid sample measure the NPs content in a different way, so the SLP for the same NP could be different in the case of the entire NP content being evaluated, instead only the Fe content or Fe-oxide content are considered. In fact, different authors have determined the magnetic material content in NP fluid in different ways as reported e.g., in [44,50–55], depending on the measurement method available.

Considering the water and octane suspensions of the C5 nanoparticle (Table 4), the generated heat is higher in the case of water. This effect can be due to the lower specific heat compared to water ($4.18 \text{ Jg}^{-1}\text{K}^{-1}$ for water and $2.238 \text{ Jg}^{-1}\text{K}^{-1}$ for octane) with a contribution due to the differences in the aggregation of nanoparticles as evidenced by their higher hydrodynamic radius.

When the same nanofluid (30 mL with 10 mg/mL of nanoparticle) is exposed to different magnetic field intensities at three different frequencies, it is evident that the heating generation increases both with the magnetic field strength and the magnetic field frequency as evidenced in Figure 9 and Table 4. Data at magnetic field value, given the field frequency, could be interpolated with a straight line with a 0-intercept.

5. Conclusions

The paper reports the evaluation of the Specific Loss Power, SLP, generated by three different types of magnetic nanoparticles, MNPs, either in octane or water suspension. The nanoparticles were synthesized according to established and reproducible procedures such as coprecipitation and thermal decomposition methods. The NPs were characterized in terms of shape, size, and chemical composition. Finally, the suspension, octane, or water, were characterized in terms of SLP using three different methods. The obtained results in the computation of the SLP were compared, and only those that analyze the initial slope showed similar results. In some cases, the exponential method failed and did not prove suitable, for instance, when secondary thermally induced phenomena such as aggregation or precipitation happen during the measurement. Nevertheless, the behavior of the heating curve is useful to evaluate the amplitude of the interval analysis for the initial slope methods. In particular, this study shows that this analysis interval cannot be fixed at equal for all the nanofluids but has to be determined for each sample.

Author Contributions: Conceptualization, P.S. and E.S.; methodology, P.S., E.S. and S.G.C.; investigation, P.S., E.S., L.D.B., F.S., S.G.C. and M.R.R.; resources, M.F. and M.M., data curation, P.S., F.S., L.D.B., E.S. and M.B.; writing—original draft preparation, E.S., F.S., L.D.B. and M.R.R.; writing—review and editing, R.B., M.M., P.S., M.F. and M.B.; supervision, M.F. All authors have read and agreed to the published version of the manuscript.

Funding: This research received no external funding.

Data Availability Statement: No data available.

Acknowledgments: Authors are grateful to Robert Ivkov and Anirudh Sharma from Johns Hopkins University, Baltimore, MD 21231, USA for the helpful discussion and some of the SW used for SLP analysis. The work was developed in the frame of the COST action CA17115—European network for advancing Electromagnetic hyperthermic medical technologies (MyWAVE, <https://www.cost.eu/actions/CA17115> (accessed on 4 September 2018)).

Conflicts of Interest: The authors declare no conflict of interest.

References

1. Jordan, A.; Scholz, R.; Wust, P.; Fahling, H.; Roland, F. Magnetic Fluid Hyperthermia (MFH): Cancer Treatment with AC Magnetic Field Induced Excitation of Biocompatible Superparamagnetic Nanoparticles. *J. Magn. Magn. Mater.* **1999**, *201*, 413–419. [[CrossRef](#)]
2. Jordan, A.; Scholz, R.; Wust, P.; Fähling, H.; Krause, J.; Wlodarczyk, W.; Sander, B.; Vogl, T.; Felix, R. Effects of Magnetic Fluid Hyperthermia (MFH) on C3H Mammary Carcinoma In Vivo. *Int. J. Hyperth.* **1997**, *13*, 587–605. [[CrossRef](#)] [[PubMed](#)]
3. Gneveckow, U.; Jordan, A.; Scholz, R.; Brüß, V.; Waldöfner, N.; Ricke, J.; Feussner, A.; Hildebrandt, B.; Rau, B.; Wust, P. Description and Characterization of the Novel Hyperthermia- and Thermoablation-System MFH 300F for Clinical Magnetic Fluid Hyperthermia. *Med. Phys.* **2004**, *31*, 1444–1451. [[CrossRef](#)]
4. Goya, G.F.; Asín, L.; Ibarra, M.R. Cell Death Induced by AC Magnetic Fields and Magnetic Nanoparticles: Current State and Perspectives. *Int. J. Hyperth.* **2013**, *29*, 810–818. [[CrossRef](#)] [[PubMed](#)]
5. Baronzio, G. A Brief Overview of Hyperthermia in Cancer Treatment. *J. Integr. Oncol.* **2014**, *3*, 115. [[CrossRef](#)]
6. Ivkov, R.; DeNardo, S.J.; Daum, W.; Foreman, A.R.; Goldstein, R.C.; Nemkov, V.S.; DeNardo, G.L. Application of High Amplitude Alternating Magnetic Fields for Heat Induction of Nanoparticles Localized in Cancer. *Clin. Cancer Res.* **2005**, *11*, 7093s–7103s. [[CrossRef](#)]
7. Rosensweig, R.E. Heating Magnetic Fluid with Alternating Magnetic Field. *J. Magn. Magn. Mater.* **2002**, *252*, 370. [[CrossRef](#)]
8. Dewhurst, M.; Stauffer, P.R.; Das, S.; Craciunescu, O.I.; Vujaskovic, Z.; Gunderson, L.; Tepper, J. Hyperthermia. In *Clinical Radiation Oncology*; Elsevier: Amsterdam, The Netherlands, 2020; pp. 381–398. ISBN 978-0-323-67246-7.
9. Fortin, J.P.; Gazeau, F.; Wilhelm, C. Intracellular Heating of Living Cells through Neel Relaxation of Magnetic Nanoparticles. *Eur. Biophys. J. EBJ* **2008**, *37*, 223–228. [[CrossRef](#)]
10. Borkamo, E.D.; Fluge, O.; Mella, O.; Akslen, L.A.; Bruland, O.; Dahl, O. Hyperthermia Improves the Antitumour Effect of Metronomic Cyclophosphamide in a Rat Transplantable Brain Tumour. *Radiother. Oncol.* **2008**, *86*, 435–442. [[CrossRef](#)]
11. Moroz, P.; Jones, S.K.; Gray, B.N. Magnetically Mediated Hyperthermia: Current Status and Future Directions. *Int. J. Hyperth.* **2002**, *18*, 267–284. [[CrossRef](#)]
12. Hildebrandt, B.; Wust, P.; Ahlers, O.; Dieing, A.; Sreenivasa, G.; Kerner, T.; Felix, R.; Riess, H. The Cellular and Molecular Basis of Hyperthermia. *Crit. Rev. Oncol. Hematol.* **2002**, *43*, 33–56. [[CrossRef](#)] [[PubMed](#)]
13. Gerweck, L.E. Hyperthermia in Cancer Therapy: The Biological Basis and Unresolved Questions. *Cancer Res.* **1985**, *45*, 3408–3414. [[PubMed](#)]
14. Dutz, S.; Hergt, R. Magnetic Nanoparticle Heating and Heat Transfer on a Microscale: Basic Principles, Realities and Physical Limitations of Hyperthermia for Tumour Therapy. *Int. J. Hyperth.* **2013**, *29*, 790–800. [[CrossRef](#)] [[PubMed](#)]
15. Jiang, W.; Bian, L.; Ma, L.-J.; Tang, R.-Z.; Xun, S.; He, Y.-W. Hyperthermia-Induced Apoptosis in Tca8113 Cells Is Inhibited by Heat Shock Protein 27 through Blocking Phospholipid Scramblase 3 Phosphorylation. *Int. J. Hyperth.* **2010**, *26*, 523–537. [[CrossRef](#)]
16. Nishikawa, H.; Kimura, T.; Kita, R.; Osaki, Y. Radiofrequency Ablation for Hepatocellular Carcinoma. *Int. J. Hyperth.* **2013**, *29*, 558–568. [[CrossRef](#)]
17. Hergt, R.; Andrä, W. Magnetic Hyperthermia and Thermoablation. In *Magnetism in Medicine: A Handbook*, 2nd ed.; John Wiley & Sons: Hoboken, NJ, USA, 2006; 550p.
18. Kozissnik, B.; Bohorquez, A.C.; Dobson, J.; Rinaldi, C. Magnetic Fluid Hyperthermia: Advances, Challenges, and Opportunity. *Int. J. Hyperth.* **2013**, *29*, 706–714. [[CrossRef](#)]
19. Krishnan, K.M. Biomedical Nanomagnetism: A Spin Through Possibilities in Imaging, Diagnostics, and Therapy. *Magn. IEEE Trans.* **2010**, *46*, 2523–2558. [[CrossRef](#)]
20. Giordano, M.A.; Gutierrez, G.; Rinaldi, C. Fundamental Solutions to the Bioheat Equation and Their Application to Magnetic Fluid Hyperthermia. *Int. J. Hyperth.* **2010**, *26*, 475–484. [[CrossRef](#)]
21. Jordan, A.; Scholz, R.; Maier-Hauff, K.; Johannsen, M.; Wust, P.; Nadobny, J.; Schirra, H.; Schmidt, H.; Deger, S.; Loening, S.; et al. Presentation of a New Magnetic Field Therapy System for the Treatment of Human Solid Tumors with Magnetic Fluid Hyperthermia. *J. Magn. Magn. Mater.* **2001**, *225*, 118–126. [[CrossRef](#)]
22. Short, J.G.; Turner, P.F. Physical Hyperthermia and Cancer Therapy. *Proc. IEEE* **1980**, *68*, 133–142. [[CrossRef](#)]
23. Brezovich, I.A.; Atkinson, W.J.; Lilly, M.B. Local Hyperthermia with Interstitial Techniques. *Cancer Res.* **1984**, *44*, 4752s–4756s.
24. Arriortua, O.K.; Garaio, E.; Herrero de la Parte, B.; Insausti, M.; Lezama, L.; Plazaola, F.; García, J.A.; Aizpurua, J.M.; Sagartazu, M.; Irazola, M.; et al. Antitumor Magnetic Hyperthermia Induced by RGD-Functionalized Fe₃O₄ Nanoparticles, in an Experimental Model of Colorectal Liver Metastases. *Beilstein J. Nanotechnol.* **2016**, *7*, 1532–1542. [[CrossRef](#)]
25. Herrero de la Parte, B.; Rodrigo, I.; Gutiérrez-Basoa, J.; Iturrizaga Correcher, S.; Mar Medina, C.; Echevarría-Uraga, J.J.; Garcia, J.A.; Plazaola, F.; García-Alonso, I. Proposal of New Safety Limits for In Vivo Experiments of Magnetic Hyperthermia Antitumor Therapy. *Cancers* **2022**, *14*, 3084. [[CrossRef](#)]
26. Lee, J.-H.; Jang, J.; Choi, J.; Moon, S.H.; Noh, S.; Kim, J.; Kim, J.-G.; Kim, I.-S.; Park, K.I.; Cheon, J. Exchange-Coupled Magnetic Nanoparticles for Efficient Heat Induction. *Nat. Nanotechnol.* **2011**, *6*, 418–422. [[CrossRef](#)] [[PubMed](#)]
27. Laurent, S.; Dutz, S.; Häfeli, U.O.; Mahmoudi, M. Magnetic Fluid Hyperthermia: Focus on Superparamagnetic Iron Oxide Nanoparticles. *Adv. Colloid Interface Sci.* **2011**, *166*, 8–23. [[CrossRef](#)] [[PubMed](#)]
28. Zeisberger, M.; Dutz, S.; Müller, R.; Hergt, R.; Matoussevitch, N.; Bönnemann, H. Metallic Cobalt Nanoparticles for Heating Applications. *J. Magn. Magn. Mater.* **2007**, *311*, 224–227. [[CrossRef](#)]

29. Hergt, R.; Dutz, S. Magnetic Particle Hyperthermia—Biophysical Limitations of a Visionary Tumour Therapy. *J. Magn. Magn. Mater.* **2007**, *311*, 187–192. [[CrossRef](#)]
30. Dutz, S.H.R. Magnetic Nanoparticles for Biomedical Heating Applications. *Z. Phys. Chem.* **2005**, *220*, 145. [[CrossRef](#)]
31. Roca, A.G.; Costo, R.; Rebolledo, A.F.; Veintemillas-Verdaguer, S.; Tartaj, P.; González-Carreño, T.; Morales, M.P.; Serna, C.J. Progress in the Preparation of Magnetic Nanoparticles for Applications in Biomedicine. *J. Phys. D Appl. Phys.* **2009**, *42*, 224002. [[CrossRef](#)]
32. Xu, C.; Sun, S. Superparamagnetic Nanoparticles as Targeted Probes for Diagnostic and Therapeutic Applications. *Dalton Trans.* **2009**, *29*, 5583–5591. [[CrossRef](#)]
33. Frey, N.A.; Peng, S.; Cheng, K.; Sun, S. Magnetic Nanoparticles: Synthesis, Functionalization, and Applications in Bioimaging and Magnetic Energy Storage. *Chem. Soc. Rev.* **2009**, *38*, 2532. [[CrossRef](#)] [[PubMed](#)]
34. Sun, S.; Zeng, H.; Robinson, D.B.; Raoux, S.; Rice, P.M.; Wang, S.X.; Li, G. Monodisperse MFe₂O₄ (M = Fe, Co, Mn) Nanoparticles. *J. Am. Chem. Soc.* **2003**, *126*, 273–279. [[CrossRef](#)] [[PubMed](#)]
35. Sun, S.; Zeng, H. Size Controlled Synthesis of Magnetite Nanoparticles. *J. Am. Chem. Soc.* **2002**, *124*, 8204. [[CrossRef](#)]
36. Borgohain, C.; Senapati, K.K.; Mishra, D.; Sarma, K.C.; Phukan, P. A New CoFe₂O₄–Cr₂O₃–SiO₂ Fluorescent Magnetic Nanocomposite. *Nanoscale* **2010**, *2*, 2250. [[CrossRef](#)]
37. Baldi, G.; Bonacchi, D.; Franchini, M.C.; Gentili, D.; Lorenzi, G.; Ricci, A.; Ravagli, C. Synthesis and Coating of Cobalt Ferrite Nanoparticles: A First Step toward the Obtainment of New Magnetic Nanocarriers. *Langmuir ACS J. Surf. Colloids* **2007**, *23*, 4026–4028. [[CrossRef](#)]
38. Goya, G.F.; Grazu, V.; Ibarra, M.R. Magnetic nanoparticles for cancer therapy. *Curr. Nanosci.* **2008**, *4*, 1–16. [[CrossRef](#)]
39. Pal, R. Fundamental Rheology of Disperse Systems Based on Single-Particle Mechanics. *Fluids* **2016**, *1*, 40. [[CrossRef](#)]
40. Darwish, M.S.A.; Kim, H.; Bui, M.P.; Le, T.-A.; Lee, H.; Ryu, C.; Lee, J.Y.; Yoon, J. The Heating Efficiency and Imaging Performance of Magnesium Iron Oxide@tetramethyl Ammonium Hydroxide Nanoparticles for Biomedical Applications. *Nanomaterials* **2021**, *11*, 1096. [[CrossRef](#)]
41. Goya, G.F.; Berquó, T.S.; Fonseca, F.C.; Morales, M.P. Static and Dynamic Magnetic Properties of Spherical Magnetite Nanoparticles. *J. Appl. Phys.* **2003**, *94*, 3520–3528. [[CrossRef](#)]
42. Natividad, E.; Castro, M.; Mediano, A. Adiabatic Magnetothermia Makes Possible the Study of the Temperature Dependence of the Heat Dissipated by Magnetic Nanoparticles under Alternating Magnetic Fields. *Appl. Phys. Lett.* **2011**, *98*, 243119. [[CrossRef](#)]
43. Natividad, E.; Castro, M.; Mediano, A. Adiabatic vs. Non-Adiabatic Determination of Specific Absorption Rate of Ferrofluids. *J. Magn. Magn. Mater.* **2009**, *321*, 1497–1500. [[CrossRef](#)]
44. Andreu, I.; Natividad, E. Accuracy of Available Methods for Quantifying the Heat Power Generation of Nanoparticles for Magnetic Hyperthermia. *Int. J. Hyperth.* **2013**, *29*, 739–751. [[CrossRef](#)] [[PubMed](#)]
45. Soetaert, F.; Kandala, S.K.; Bakuzis, A.; Ivkov, R. Experimental Estimation and Analysis of Variance of the Measured Loss Power of Magnetic Nanoparticles. *Sci. Rep.* **2017**, *7*, 6661. [[CrossRef](#)] [[PubMed](#)]
46. Wildeboer, R.R.; Southern, P.; Pankhurst, Q.A. On the Reliable Measurement of Specific Absorption Rates and Intrinsic Loss Parameters in Magnetic Hyperthermia Materials. *J. Phys. D Appl. Phys.* **2014**, *47*, 495003. [[CrossRef](#)]
47. Lahiri, B.B.; Ranoo, S.; Philip, J. Uncertainties in the Estimation of Specific Absorption Rate during Radiofrequency Alternating Magnetic Field Induced Non-Adiabatic Heating of Ferrofluids. *J. Phys. D Appl. Phys.* **2017**, *50*, 455005. [[CrossRef](#)]
48. Bordelon, D.E.; Cornejo, C.; Grüttner, C.; Westphal, F.; DeWeese, T.L.; Ivkov, R. Magnetic Nanoparticle Heating Efficiency Reveals Magneto-Structural Differences When Characterized with Wide Ranging and High Amplitude Alternating Magnetic Fields. *J. Appl. Phys.* **2011**, *109*, 124904. [[CrossRef](#)]
49. Pavel, M.; Stancu, A. Ferromagnetic Nanoparticles Dose Based on Tumor Size in Magnetic Fluid Hyperthermia Cancer Therapy. *Magn. IEEE Trans.* **2009**, *45*, 5251–5254. [[CrossRef](#)]
50. Dennis, C.L.; Ivkov, R. Physics of Heat Generation Using Magnetic Nanoparticles for Hyperthermia. *Int. J. Hyperth.* **2013**, *29*, 715–729. [[CrossRef](#)]
51. Martinez-Boubeta, C.; Simeonidis, K.; Makridis, A.; Angelakeris, M.; Iglesias, O.; Guardia, P.; Cabot, A.; Yedra, L.; Estradé, S.; Peiró, F.; et al. Learning from Nature to Improve the Heat Generation of Iron-Oxide Nanoparticles for Magnetic Hyperthermia Applications. *Sci. Rep.* **2013**, *3*, 1652. [[CrossRef](#)]
52. Urtizberea, A.; Natividad, E.; Arizaga, A.; Castro, M.; Mediano, A. Specific Absorption Rates and Magnetic Properties of Ferrofluids with Interaction Effects at Low Concentrations. *J. Phys. Chem. C* **2010**, *114*, 4916–4922. [[CrossRef](#)]
53. De la Presa, P.; Luengo, Y.; Multigner, M.; Costo, R.; Morales, M.P.; Rivero, G.; Hernando, A. Study of Heating Efficiency as a Function of Concentration, Size, and Applied Field in γ -Fe₂O₃ Nanoparticles. *J. Phys. Chem. C* **2012**, *116*, 25602–25610. [[CrossRef](#)]
54. Tomitaka, A.; Ueda, K.; Yamada, T.; Takemura, Y. Heat Dissipation and Magnetic Properties of Surface-Coated Fe₃O₄ Nanoparticles for Biomedical Applications. *J. Magn. Magn. Mater.* **2012**, *324*, 3437–3442. [[CrossRef](#)]
55. Branquinho, L.C.; Carrião, M.S.; Costa, A.S.; Zufelato, N.; Sousa, M.H.; Miotto, R.; Ivkov, R.; Bakuzis, A.F. Effect of Magnetic Dipolar Interactions on Nanoparticle Heating Efficiency: Implications for Cancer Hyperthermia. *Sci. Rep.* **2013**, *3*, 2887. [[CrossRef](#)] [[PubMed](#)]
56. Ghasemi, E.; Mirhabibi, A.; Edrissi, M. Synthesis and Rheological Properties of an Iron Oxide Ferrofluid. *J. Magn. Magn. Mater.* **2008**, *320*, 2635–2639. [[CrossRef](#)]
57. ImageJ. Available online: <http://imagej.nih.gov/ij/> (accessed on 3 October 2014).

58. Ruggiero, M.R.; Crich, S.G.; Sieni, E.; Sgarbossa, P.; Forzan, M.; Cavallari, E.; Stefania, R.; Dughiero, F.; Aime, S. Magnetic Hyperthermia Efficiency and $^1\text{H-NMR}$ Relaxation Properties of Iron Oxide/Paclitaxel-Loaded PLGA Nanoparticles. *Nanotechnology* **2016**, *27*, 285104. [[CrossRef](#)]
59. Spizzo, F.; Sgarbossa, P.; Sieni, E.; Semenzato, A.; Dughiero, F.; Forzan, M.; Bertani, R.; Del Bianco, L. Synthesis of Ferrofluids Made of Iron Oxide Nanoflowers: Interplay between Carrier Fluid and Magnetic Properties. *Nanomaterials* **2017**, *7*, 373. [[CrossRef](#)]
60. Di Barba, P.D.; Dughiero, F.; Sieni, E. Magnetic Field Synthesis in the Design of Inductors for Magnetic Fluid Hyperthermia. *Magn. IEEE Trans.* **2010**, *46*, 2931–2934. [[CrossRef](#)]
61. Bertani, R.; Ceretta, F.; Barba, P.D.; Dughiero, F.; Forzan, M.; Michelin, R.A.; Sgarbossa, P.; Sieni, E.; Spizzo, F. Optimal Inductor Design for Nanofluid Heating Characterisation. *Eng. Comput.* **2015**, *32*, 1870–1892. [[CrossRef](#)]
62. Van de Hulst, H.C. *Light Scattering by Small Particles*; Dover Publications: New York, NY, USA, 1981; ISBN 978-0-486-64228-4.
63. Bohren, C.F.; Huffman, D.R. *Absorption and Scattering of Light by Small Particles*; Wiley-VCH: Weinheim, Germany, 2004; ISBN 978-0-471-29340-8.
64. Cullity, B.D.; Graham, C.D. *Introduction to Magnetic Materials*, 2nd ed.; IEEE/Wiley: Hoboken, NJ, USA, 2009; ISBN 978-0-471-47741-9.
65. Coey, J.M.D. Noncollinear Spin Arrangement in Ultrafine Ferrimagnetic Crystallites. *Phys. Rev. Lett.* **1971**, *27*, 1140–1142. [[CrossRef](#)]
66. Coduri, M.; Masala, P.; Del Bianco, L.; Spizzo, F.; Ceresoli, D.; Castellano, C.; Cappelli, S.; Oliva, C.; Checchia, S.; Allieta, M.; et al. Local Structure and Magnetism of Fe_2O_3 Maghemite Nanocrystals: The Role of Crystal Dimension. *Nanomaterials* **2020**, *10*, 867. [[CrossRef](#)]
67. Morales, M.P.; Veintemillas-Verdaguer, S.; Montero, M.I.; Serna, C.J.; Roig, A.; Casas, L.; Martínez, B.; Sandiumenge, F. Surface and Internal Spin Canting in $\gamma\text{-Fe}_2\text{O}_3$ Nanoparticles. *Chem. Mater.* **1999**, *11*, 3058–3064. [[CrossRef](#)]
68. Parker, F.T.; Foster, M.W.; Margulies, D.T.; Berkowitz, A.E. Spin Canting, Surface Magnetization, and Finite-Size Effects in $\gamma\text{-Fe}_2\text{O}_3$ Particles. *Phys. Rev. B* **1993**, *47*, 7885–7891. [[CrossRef](#)]
69. Zhen, G.; Muir, B.W.; Moffat, B.A.; Harbour, P.; Murray, K.S.; Moubaraki, B.; Suzuki, K.; Madsen, I.; Agron-Olshina, N.; Waddington, L.; et al. Comparative Study of the Magnetic Behavior of Spherical and Cubic Superparamagnetic Iron Oxide Nanoparticles. *J. Phys. Chem. C* **2011**, *115*, 327–334. [[CrossRef](#)]
70. Luigies, B.; Woudenberg, S.M.C.; de Groot, R.; Meeldijk, J.D.; Torres Galvis, H.M.; de Jong, K.P.; Philipse, A.P.; Erné, B.H. Diverging Geometric and Magnetic Size Distributions of Iron Oxide Nanocrystals. *J. Phys. Chem. C* **2011**, *115*, 14598–14605. [[CrossRef](#)]
71. Del Bianco, L.; Spizzo, F.; Barucca, G.; Ruggiero, M.R.; Geninatti Crich, S.; Forzan, M.; Sieni, E.; Sgarbossa, P. Mechanism of Magnetic Heating in Mn-Doped Magnetite Nanoparticles and the Role of Intertwined Structural and Magnetic Properties. *Nanoscale* **2019**, *11*, 10896–10910. [[CrossRef](#)]
72. Yang, L.; Ma, L.; Xin, J.; Li, A.; Sun, C.; Wei, R.; Ren, B.W.; Chen, Z.; Lin, H.; Gao, J. Composition Tunable Manganese Ferrite Nanoparticles for Optimized T_2 Contrast Ability. *Chem. Mater.* **2017**, *29*, 3038–3047. [[CrossRef](#)]
73. Giri, J.; Pradhan, P.; Sriharsha, T.; Bahadur, D. Preparation and Investigation of Potentiality of Different Soft Ferrites for Hyperthermia Applications. *J. Appl. Phys.* **2005**, *97*, 10Q916. [[CrossRef](#)]
74. Dormann, J.L.; Fiorani, D.; Tronc, E. Magnetic Relaxation in Fine-Particle Systems. In *Advances in Chemical Physics*; Prigogine, I., Rice, S.A., Eds.; John Wiley & Sons, Inc.: Hoboken, NJ, USA, 2007; pp. 283–494; ISBN 978-0-470-14157-1.
75. Blanco-Mantecón, M.; O’Grady, K. Interaction and Size Effects in Magnetic Nanoparticles. *J. Magn. Magn. Mater.* **2006**, *296*, 124–133. [[CrossRef](#)]
76. Burrows, F.; Parker, C.; Evans, R.F.L.; Hancock, Y.; Hovorka, O.; Chantrell, R.W. Energy Losses in Interacting Fine-Particle Magnetic Composites. *J. Phys. D Appl. Phys.* **2010**, *43*, 474010. [[CrossRef](#)]
77. Ovejero, J.G.; Spizzo, F.; Morales, M.P.; Del Bianco, L. Nanoparticles for Magnetic Heating: When Two (or More) Is Better Than One. *Materials* **2021**, *14*, 6416. [[CrossRef](#)]
78. El-Hilo, M.; O’Grady, K.; Chantrell, R.W. Susceptibility Phenomena in a Fine Particle System. *J. Magn. Magn. Mater.* **1992**, *114*, 295–306. [[CrossRef](#)]
79. Binns, C.; Maher, M.J.; Pankhurst, Q.A.; Kechrakos, D.; Trohidou, K.N. Magnetic Behavior of Nanostructured Films Assembled from Preformed Fe Clusters Embedded in Ag. *Phys. Rev. B* **2002**, *66*, 184413. [[CrossRef](#)]
80. Coral, D.F.; Mendoza Zélis, P.; Marciello, M.; Morales, M.d.P.; Craievich, A.; Sánchez, F.H.; Fernández van Raap, M.B. Effect of Nanoclustering and Dipolar Interactions in Heat Generation for Magnetic Hyperthermia. *Langmuir* **2016**, *32*, 1201–1213. [[CrossRef](#)] [[PubMed](#)]
81. Del Bianco, L.; Lesci, I.G.; Fracasso, G.; Barucca, G.; Spizzo, F.; Tamisari, M.; Scotti, R.; Ciocca, L. Synthesis of Nanogranular Fe_3O_4 /Biomimetic Hydroxyapatite for Potential Applications in Nanomedicine: Structural and Magnetic Characterization. *Mater. Res. Express* **2015**, *2*, 065002. [[CrossRef](#)]
82. Bedanta, S.; Kleemann, W. Supermagnetism. *J. Phys. D Appl. Phys.* **2009**, *42*, 013001. [[CrossRef](#)]
83. Dormann, J.L.; Cherkaoui, R.; Spinu, L.; Noguès, M.; Lucari, F.; D’Orazio, F.; Fiorani, D.; Garcia, A.; Tronc, E.; Jolivet, J.P. From Pure Superparamagnetic Regime to Glass Collective State of Magnetic Moments in $\gamma\text{-Fe}_2\text{O}_3$ Nanoparticle Assemblies. *J. Magn. Magn. Mater.* **1998**, *187*, L139–L144. [[CrossRef](#)]

84. Del Bianco, L.; Spizzo, F.; Barucca, G.; Marangoni, G.; Sgarbossa, P. Glassy Magnetic Behavior and Correlation Length in Nanogranular Fe-Oxide and Au/Fe-Oxide Samples. *Materials* **2019**, *12*, 3958. [[CrossRef](#)]
85. Ring, H.L.; Sharma, A.; Ivkov, R.; Bischof, J.C. The Impact of Data Selection and Fitting on SAR Estimation for Magnetic Nanoparticle Heating. *Int. J. Hyperth.* **2020**, *37*, 100–107. [[CrossRef](#)]

Disclaimer/Publisher’s Note: The statements, opinions and data contained in all publications are solely those of the individual author(s) and contributor(s) and not of MDPI and/or the editor(s). MDPI and/or the editor(s) disclaim responsibility for any injury to people or property resulting from any ideas, methods, instructions or products referred to in the content.